optica

Boosting optical nonreciprocity: surface reconstruction in iron garnets

Sushree S. Dash,[1] Pinaki Mukherjee,[2] Daniel Haskel,[3] Richard A. Rosenberg,[3] and Miguel Levy[1,2,*]

[1]Physics Department, Michigan Technological University, Houghton, Michigan 49931, USA
[2]Materials Science Department, Michigan Technological University, Houghton, Michigan 49931, USA
[3]Argonne National Laboratory, Advanced Photon Source, Lemont, Illinois 60439, USA
*Corresponding author: mlevy@mtu.edu

Received 27 May 2020; revised 24 July 2020; accepted 28 July 2020 (Doc. ID 398732); published 24 August 2020

Bi-substituted iron garnet films are extensively used in the fabrication of nonreciprocal devices in optical telecommunications. The miniaturization of these devices for on-chip integration requires the development of more efficient magneto-optic materials than presently available. Recent evidence has emerged of large near-surface enhancements in the magneto-optic response in these materials. However, their operative mechanisms at the atomic and electronic levels are not as yet understood. We report significant differences in the ionic structure between surface and bulk in bismuth-substituted iron garnet materials. It is found that the unit cell is elongated normal to the surface, thus enlarging the separation between Fe^{3+} ions. These ions play a central role in the magneto-optic response of this material. A marked displacement of Fe ions creates gaps at the surface that are populated in the bulk. Concomitantly, surface- and bulk-sensitive measurements of spin-polarized 3d Fe^{3+} states show significant differences in the magnitude of L_2 edge x-ray magnetic circular dichroism, as well as differences in L_3 edge dichroism, which, in the presence of spin-orbit coupling in 3d states, can be assigned to high-energy states. An increase in magnetic circular dichroism correlates with larger Faraday rotation. These findings provide a deeper understanding of the role of the surface in the electronic transitions to excited Fe^{3+} 3d states, responsible for these nonreciprocal phenomena. Together with the surface reconstruction underlying these effects reported here, they provide a useful tool for the further development of improved materials technologies to advance the integration of nonreciprocal devices in optical circuits.

https://doi.org/10.1364/OPTICA.398732

1. INTRODUCTION

Recent work on the magneto-optic response of bismuth-substituted iron garnet films has uncovered a multifold enhancement in Faraday rotation below 50 nm thick films [1–3]. Classical electromagnetic analysis of the experimental data has been used to trace this unexpected effect to the contribution of the surface [1–3]. The data are consistent with a sevenfold increase in the Faraday effect within 2 nm of the surface at 532 nm wavelength [1].

In order to explore the microscopic origins of this effect, the present work focuses on a comparative study of the crystallographic- and electronic-structure differences between surface and bulk in these types of garnets. Relatively thick 2 μm thick films are used to eliminate any film–substrate interfacial contributions to the data on electronic transitions in Fe^{3+} ions in order to isolate the surface and bulk contributions from that of the substrate interface. Iron ions play a central role in the magneto-optic response of these garnets.

Bismuth-substituted iron garnets are technologically important materials, used in the fabrication of nonreciprocal optical devices such as isolators and circulators. These components are widely used in the telecommunications industry for the protection of laser sources from back-reflected light. The miniaturization of these devices and their integration into on-chip optical circuits constitutes a driver for the development of more efficient magneto-optic materials than presently available. Magneto-optic effects in the near-infrared regime are controlled by a small parameter, the nonreciprocal gyrotropy. The need to boost up its magnitude is ever present in this continually developing field [4–10].

Bismuth- and cerium-substitution techniques proved effective more than two decades ago [4–6]. Subsequent efforts through photonic crystal and ring-resonator technologies made further advances, but with accompanying drawbacks in bandwidth [11–23]. No further advances of disruptive significance have occurred since. Hence, bringing to bear relatively unexplored surface effects to leverage the Faraday response in nanoscale nonreciprocal devices is important at this time given the recent evidence revealed in Refs. [1–3]. The point of this paper is to communicate

the operative mechanisms at the atomic and electronic levels at the surface so that they may be applied to practical devices and developed further through improved materials technologies.

Motivated by the results in Refs. [1–3], the authors have conducted a comparative analysis of the ionic structure in the bulk and the surface of these films. This study was performed via scanning transmission electron microscopy (S-TEM). Iron garnets belong to the space group $Ia3d$ (O_h^{10}). They contain three sublattices, two with Fe^{3+} ions in tetrahedral and octahedral coordination with surrounding O^{2-} ions and one with bismuth and lutetium ions in dodecahedral coordination with the oxygen ions. The study shows that the bulk conforms with a perfect $Ia3d$ structural symmetry, but the near-surface ionic structure is distorted away from bulk symmetry. Such distortions are consistent with electronic energy level splitting and changes in the density of 3d Fe^{3+} states, evidence of which is found in Fe L-edge x-ray absorption spectroscopy (XAS) and x-ray magnetic circular dichroism (XMCD) measurements reported here.

In Bi-substituted iron garnet systems, the ground state for optical transitions is an orbital-singlet state consisting of spin-exchange-coupled Fe^{3+} 3d electrons, in both tetrahedral and octahedral sublattices [7]. The excited state is an orbital triplet. In this state, the excited Fe^{3+} spin magnetic moment is captured by the exchange field, but the orbital degeneracy is lifted by a strong spin-orbit coupling due to the contributions from the large Bi^{3+} spin–orbit interaction [7]. The Fe^{3+} and Bi^{3+} form hybrid excited states.

Three main structural features emerge from a comparison of surface and bulk crystallography. (1) The distance between unit cells in the out-of-plane (normal to the surface) direction is slightly reduced at the surface, but not in the plane of the film, as compared to the bulk. (2) The distance between Fe ions at the ends of each unit cell is increased in the out-of-plane direction but remains the same in the direction parallel to the surface. (3) There is a marked absence of Fe ions in the middle of the three-ion square edges of the unit cell in the surface as compared to the bulk.

To complement this structural study, we have conducted an experimental study of the differences in XAS and XMCD between the surface and the bulk in these types of films. This study is based on a comparison between total fluorescence yield (TFY) and total electron yield (TEY). The former probes the bulk response, and the latter probes the surface response. However, due to limitations in the accepted analytical corrections to bring fluorescence yield in conformity with x-ray absorption, these differences between the surface and bulk electronic response will need to be confirmed with additional measurements.

The Faraday effect originates from differences in absorption between right- and left-circularly polarized photons, i.e., magnetic circular dichroism, in the optical regime. At the same time, XAS and XMCD in iron garnets are able to probe differences in the electronic structure of the surface and of the bulk of the material. Hence, they allow one to ascertain the presence of differences in the electronic levels and density of states that participate in the Faraday effect as a result of surface symmetry breaking and surface reconstruction.

A key feature emerges from the x-ray analysis. The L-edge XMCD data exhibits a possible reconfiguration of available 3d states away from lower and towards higher angular momenta normal components (along the direction of the magnetic field) in the surface as compared to the bulk. A larger magnetic circular dichroism is a signature of enhanced Faraday rotation involving those states.

2. ANALYTICAL METHODS

A. Scanning Transmission Electron Microscopy

These measurements were performed on 2 μm thick $Bi_{0.7}Gd_{0.2}Lu_2Fe_{4.3}Ga_{0.7}O_{12}$ films grown by liquid-phase epitaxy on (001)-oriented $Gd_3Ga_5O_{12}$ substrates. Samples used in these experiments were analyzed via scanning-transmission-electron microscopy (S-TEM). The purpose of this analysis was to determine differences between surface and bulk crystallographic structures in these materials and any compositional differences. Film cross sections were prepared and thinned down using the focused ion beam (FIB) method. The imaging and spectroscopic measurements of the surface and the interior of the film was performed in scanning mode of the TEM, with a point resolution of 0.8 Å.

The composition of the films was measured using energy dispersive spectroscopic mapping at the atomic scale to quantify the atomic arrangements at the bulk and surface. Iron and lutetium elemental maps from the bulk and the surface of the sample were performed, showing an approximately six-atomic-percentage decrease in Fe content at the surface compared to the bulk and a similar amount of increase in O content. All other elements show no significant variation.

There is considerable amount of overlap between Fe and Lu positions, indicating movement of these elements from their original sites at the surface. This is also corroborated by comparing the change in intensities of Fe and Fe-Lu sites at the bulk and the surface. Instrumental details are described in the section on experimental techniques at the end of the article.

B. XAS and XMCD

XAS and XMCD measurements were performed at the Argonne National Laboratory-Advanced Photon Source (ANL-APS) beamline 4-ID-C. Circularly polarized x-ray photons were used to probe the 3d shell of Fe^{3+} electrons via L-edge 2p to 3d transitions. XMCD measures the difference in absorption between right- and left-circularly polarized photons, and thus probe the difference between spin-up and spin-down unoccupied 3d states. The two L edges, L_2 and L_3, correspond to transitions from the $j = 1/2$ and $j = 3/2$ core states, respectively. In the probed energy range, these absorption processes are not only element specific (Fe) but also orbital specific (3d). The Faraday effect in the visible and infrared ranges in iron garnets is determined by absorption involving 3d electrons in iron. Thus, probing the density of available 3d states yields direct information on the electronic processes responsible for the Faraday effect in these materials.

To analyze the electronic transitions involving surface states, we measured XAS/XMCD in total electron yield (TEY) drain-current mode, which has ∼5 nm probing depth [24–26]. For bulk transitions, we measured XAS/XMCD in total fluorescence yield (TFY) mode, which has ∼50 nm probing depth. The TEY and TFY measurements were carried out simultaneously, with the latter using an energy dispersive "vortex" detector. The spectra were normalized using the TEY signal from a 70% transmitting Au mesh inserted into the photon beam. Note that, for our 2 μm thick samples, TEY and TFY are insensitive to the film–substrate interface

region due to their limited probing depth. So this methodology has the potential to yield a direct comparison of bulk and surface electronic response without any contribution from the substrate or the film–substrate interface.

Data were collected at room temperature in the presence of a 5 kOe magnetizing field parallel to the incident beam, at angles of incidence from the normal to 60° to the film surface, in steps of 10°. The applied field saturates the magnetization in these materials. The samples were mounted to an electrically isolated sample holder using double-sided carbon tape, and the surface region was grounded to the holder using silver paint. The holder was isolated from the main body of the manipulator with a sapphire disk, and the TEY signal was obtained by measuring the restoring current to the holder.

3. RESULTS AND ANALYSIS

A. Ionic Structure Differences between Bulk and Surface

Figure 1 shows the high-angle-annular-dark-field (HAADF) S-TEM images for bulk and surface in our films, oriented along the [001] zone axis. Along this zone axis, the atoms are arranged as shown in Fig. 2. Lu, Bi, Fe, and Ga atoms occupy the center of the arrangement. We denote this center site as A. This site is surrounded by three atoms along each of the four faces of a square pattern. For the purposes of the present article, we will denote each repeating square unit (or distorted-square unit, at the surface) as a unit cell.

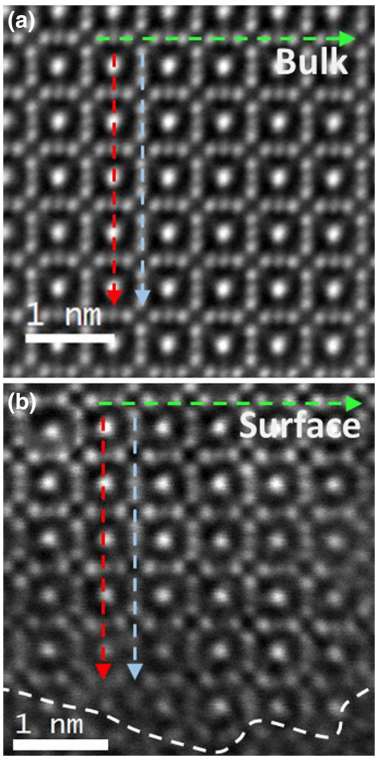

Fig. 1. HAADF scan from (a) the bulk and (b) the surface. These scans show that the regular crystalline arrangement of the bulk is modified at the surface with vacancies and distortions in the unit cell. The dashed line contour denotes the top of the surface. The unevenness of this contour is an artifact of the film-thin-down fabrication process via FIB for S-TEM analysis.

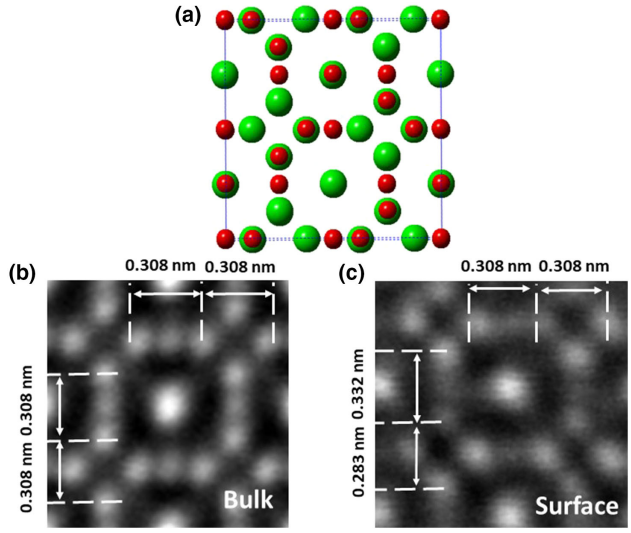

Fig. 2. (a) Atomic arrangement in the iron garnet samples projected along the [001] zone axis. The red spheres denote the combined Fe and Ga ions, and the green spheres denote the combined Bi and Lu atoms. These magnified portions of Fig. 1 show the unit cell from (b) the bulk and (c) the surface. The regular cubic symmetry of the bulk is lost at the surface.

In this arrangement of three sites, constituting the sides of the unit cell, Fe and Ga occupy the middle position exclusively, denoted here as site B. Lu, Bi, Fe, and Ga occupy the other two sites in this arrangement of three sites, denoted as sites C. In Fig. 2(a), the red spheres represent the combined Fe and Ga atoms, whereas green spheres represent the combined Lu and Bi atoms. Sites C alternate red (Fe, Ga) and green (Bi, Lu) spheres in the direction normal to the plane of the page.

Figures 2(b) and 2(c) show the relevant magnified portions of Figs. 1(a) and 1(b), depicting these kinds of arrangement for bulk and surface, respectively. As seen in Fig. 1(a), the bulk shows clear repetition of the unit cell pattern, with both the length of the three-site unit and the distance between them equal to 0.308 nm. This is true for the atomic arrangements for all four sides of the unit cell in the bulk. The fourfold cubic symmetry is preserved here.

In Fig. 2(c), which shows the corresponding ionic arrangement for the surface, the two vertical sides of the unit cell, in the direction of the depth of the film, have a slightly distorted ionic arrangement. Here the length of the three-ion unit has increased to 0.321 nm, while the distance between the units has decreased to 0.294 nm. The same arrangement at the horizontal sides of the square, parallel to the film surface, remain the same as that for the bulk. Therefore, the cubic symmetry is lost here.

The contrast in a HAADF S-TEM image is proportional to $Z^{2-\delta}$ [27,28]. Z is the atomic number of the atoms in each ion column, and δ is a correction factor that takes into consideration the detector parameters. A line scan across the ion columns reveals the variation in number of ions between them. We have drawn three line scans shown in red, blue, and green lines in Figs. 1(a) and 1(b). The corresponding normalized intensity plots are shown in the same colors in Figs. 3(a)–3(c) (bulk) and Figs. 3(d)–3(f) (surface). The red dotted line passes along the center of the arrangement (site A) mentioned in the previous paragraph. In the bulk, the ratio between site B (containing only Fe and Ga, red circles) and site A [containing Bi and Lu (green circles) and Fe and Ga (red circles)] is 0.4. At the surface, the ratio varies from 0.3–0.7, indicating

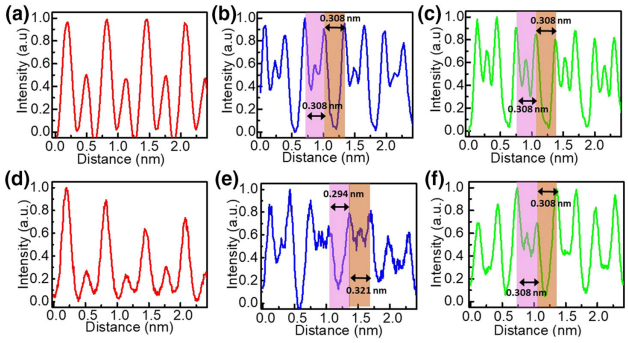

Fig. 3. Normalized intensity profile of HAADF scans along the red, blue, and green lines drawn in Fig. 1. The (a)–(c) upper and (d)–(e) lower rows are from the bulk and surface regions, respectively. As the contrast in HAADF is proportional to $Z^{2-\delta}$, the line profiles show the variation in intensity, i.e, the atomic number in each atom column.

strong nonuniform change in both of these sites. The blue line is drawn along the vertical side of the square pattern of the three-site arrangement. It clearly shows the large variations in number of ions in both sites B and C at the surface in comparison to the uniform distribution at the bulk. The intensity ratio between sites A and B in the surface varies from 0.6–0.8 compared to a steady value of 0.6 of the same in the bulk.

The green dotted line is drawn across the horizontal three-site arrangement. The line scans show similar behavior as seen in the case of blue lines. The intensity ratio between the B and C sites varies from 0.3–0.7 compared to a uniform ratio of 0.6 at the bulk. The intensity of the B sites at the surface plot does not, in most cases, go to zero, indicating again that the B sites, containing Fe/Ga atoms, have not completely disappeared at the surface. From the line scans, we clearly observe the breaking of cubic symmetry at the surface accompanied by loss of atoms in both the B and C sites. The loss in the B sites, however, is more compared to that of the C sites.

It is clear from Fig. 3 that along sides of the square, in both the vertical and horizontal directions, the Fe/Ga column (site B) is largely absent in the middle of the squares. Here it must be mentioned that, although the plot at the surface does not clearly show the B sites, their intensity is not always zero. This indicates that B sites, i.e., Fe/Ga atoms, have not completely disappeared at the surface.

Finally, as discussed in Supplement 1, the overall relative atomic content in the film shifts at the surface in comparison to that of the bulk. There is a decrease in Bi content per formula unit (pfu) at the surface, from 0.7 to 0.5, and in iron content, from 4.3 to 4.0. This implies that the increase in specific Faraday rotation near the surface reported in Refs. [1–3] is not due to an increase in Bi or Fe content. Bismuth substitution has been found to increase the Faraday response in iron garnets [4]. Additionally, at the surface we see a broadening of Lu and Fe positions in energy dispersive x-ray spectroscopy (EDS) line scans and a change in their relative intensities compared to the bulk, indicating movement of Fe and Lu ions from their respective positions. This corroborates the observation obtained from the line scans of HAADF images discussed in Fig. 3.

B. Electronic Transitions

The Faraday rotation is directly proportional to the difference in refractive indices between the right- (RCP) and left- (LCP) circular

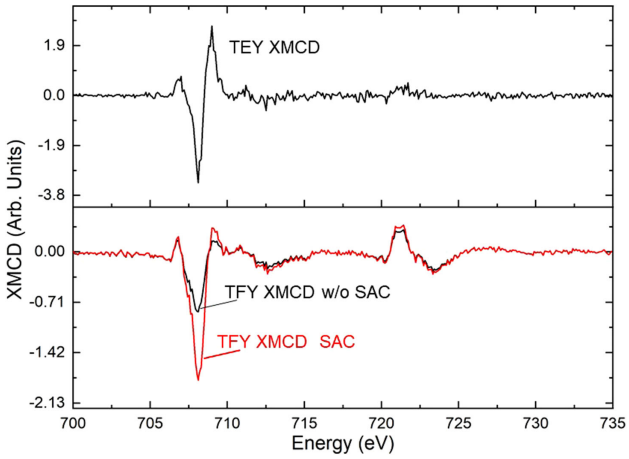

Fig. 4. TEY and TFY XMCD normalized to the incident beam flux. TFY data are shown with and without self-absorption correction (SAC). Note the relative suppression of the L_2 edge in the TEY data and the relative enhancement of the magnetic circular dichroism at the highest energy L_3 edge peak (709 eV). Our assignment of these differences to differences between surface and bulk states relies on an accurate self-absorption correction and absence of significant emission-dichroism effects in the TFY signal.

polarization components, $n_+ - n_-$, of linearly polarized light traversing a material magnetized in the direction of propagation of the optical beam. This difference, in turn, depends on the difference in the respective absorption coefficients, α_+ and α_-, through the Kramers–Kronig relations [29]. Differences in optical absorption in the dark regions of the spectrum thus translate into differences in refractive indices in transparent regions. The difference between 3d Fe^{3+} spin-up and spin-down filled and empty states in their respective density of states distributions, together with the corresponding electronic transition probabilities, controls the magneto-optic response in these materials.

Figure 4 displays the XMCD spectra for TEY (near surface) and TFY (bulk) in our samples, normalized to the incident flux. It is immediately obvious from this figure that the L_2 edge XMCD signal (720–725 eV) is significantly suppressed near the surface (TEY) compared to the bulk (TFY). These are electronic transitions from the $2p_{1/2}$ Fe core states to the 3d outer shell. On the other hand, the L_3 XMCD TEY signal (705–710 eV) corresponding to transitions from the $2p_{3/2}$ shows an enhancement in the positive 709 eV peak.

The TFY data is affected by self-absorption, namely, attenuation of outgoing fluorescence as well as changes in probing depth as the absorption coefficient changes across the edge. Data for each helicity must be corrected to account for self-absorption, considering elemental cross sections for x-ray absorption, elemental composition of the sample, and angles of incidence and detection [30]. While the self-absorption correction (SAC) enhances the L_3 relative to the L_2 XMCD signals, the line shapes remain rather unaltered, and a sizable L_2 XMCD signal remains visible (Fig. 4).

Room-temperature TEY $L_{2,3}$ XMCD data have also been reported for $Gd_3Fe_5O_{12}$, another type of iron garnet material, in Ref. [31]. Our samples differ from the latter by the presence of Bi and Lu in the dodecahedral sites, and 14% Ga substitution in the Fe sites. The most interesting feature is the larger magnetic circular dichroism in our samples at the high energy end (709 eV) of the L_3 signal as compared to $Gd_3Fe_5O_{12}$. The presence of Bi in the

dodecahedral sites significantly splits the L = 1 excited states due to the spin-orbit splitting from hybridization between the Bi and Fe levels [7]. The Bi induces a large spin-orbit splitting in the excited states, which significantly affects the Faraday rotation. In the presence of spin-orbit coupling, the absorption at the L_3 edge (j = 3/2) preferentially probes empty 3d states with j = 5/2 character, i.e., the highest energy empty 3d states.

It is known that fluorescence detection may result in fine structure that deviates from that of the true XMCD absorption spectra as a result of the latter depending only on the polarized empty density of states and the former depending on both polarized empty and filled density of states [32,33]. In the presence of spin-orbit coupling, it is predicted that the L_2 TFY magnetic circular dichroism intensity is enhanced relative to its counterpart in the XMCD absorption channel [32]. This is because the 3d states with j = 3/2 character, accessed in the L_2 absorption process, will be preferentially filled (lower energy), suppressing the absorption while enhancing the emission cross sections. While the self-absorption correction takes care of nonlinearity between the absorption and emission processes, it does not correct for additional dichroic effects in the emission channel. Although the self-absorption correction of TFY data modifies the L_3/L_2 XMCD ratio (Fig. 4), the L_2 XMCD remains sizable and much more intense than the L_2 TEY XMCD signal. The enhancement of the L_2 XMCD signal in the TFY channel is indicative of either a difference in electronic structure between surface and bulk or presence of spin-orbit interaction in the Fe 3d states, which preferentially enhances the L_2 XAS intensity in the emission channel [32].

Since spin flips are forbidden in electric dipole transitions, spin-up (spin-down) photoelectrons from the 2p core shell can only be excited into spin-up (spin-down) 3d hole states. Hence, the spin-split valence shell acts as a detector for the available angular momentum states of the excited photoelectrons, and the transition intensity is simply proportional to the number of empty 3d states of a given spin. So, assuming that additional dichroic effects in the emission channel do not alter the TFY line shape relative to that of TEY, the suppression of the L_2 signal and the enhancement of the 709 to 707 eV peak ratio in the XMCD data exhibit a reconfiguration of available 3d states away from lower and towards higher angular momenta normal components (along the direction of the magnetic field) in the surface as compared to the bulk. $2p_{1/2}$ electrons are excited into $m_j = \pm\frac{3}{2}$, 3d states, whereas $2p_{3/2}$ electrons are excited into $m_j = \pm\frac{5}{2}, \pm\frac{3}{2}$, 3d states. We conjecture based on these results that, subject to the caveats regarding the self-absorption correction expressed above, it is the higher-energy available states that dominate the Faraday response near the surface.

While these excited states are multi-electron states, the enhancement (suppression) of the surface XMCD signal seen in L_3 (L_2) TEY spectra must involve 3d electron states with enhanced $m_j = \pm\frac{5}{2}$ character, since those states are only accessible at the L_3 excitation. That the enhancement of the L_3 XMCD TEY signal occurs in the high-energy side (709 eV) is consistent with expectations from spin-orbit effects, since states with j = 5/2 character are expected to be higher in energy than those with j = 3/2 character.

Notice that there is also a shift in the XMCD L_3 edge positive and negative peak-intensity ratios from TFY and TEY. The higher energy peak at 709 eV exhibits a larger value in the TEY data than in the TFY data, and so does the lower energy peak at 707 eV. But the ratio between the 707 eV and 709 eV peak intensities decreases

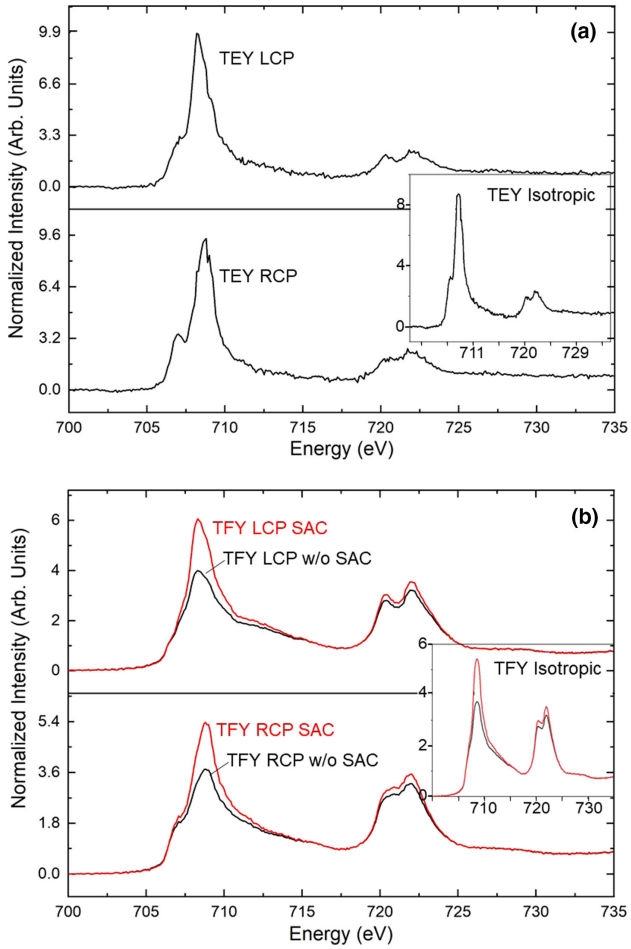

Fig. 5. Polarization-dependent XAS (a) TEY and (b) TFY data. The fine structure at the onset of the L3 edge has a much more clearly resolved multiplet structure in the RCP TEY than the RCP TFY data. The insets show the corresponding isotropic spectra, given by the sum average of the RCP and LCP spectra.

in the TEY data. This difference is either due to a shift towards higher energies in the XMCD response near the surface or to the result of emission dichroism effects (which are not accounted for in the self-absorption correction).

At the same time, there is a corresponding evolution in the L_3 RCP XAS spectra, shown in Fig. 5. The surface (TEY) RCP spectral peak near 709 eV [Fig. 5(a)] sharpens up relative to the corresponding RCP peak in the TFY data [Fig. 5(b)], revealing the secondary peak at 707 eV. This secondary peak appears as a shoulder in the broader RCP TFY spectrum. This sharpening up is either a signature that there is a stronger RCP photon absorption and longer lived electronic excitations at the higher energy, or the result of emission dichroism effects altering the TFY line shape.

The multiplet structure in the XAS TEY and TFY spectra is consistent with Fe^{3+} ($3d^5$) ions [34]. The 3 + Fe valence was verified via electron energy loss spectroscopy (EELS). Figure 6 shows the Fe L edge EELS spectra in cross-sectional samples of the iron garnet films taken with a step size of 1 nm from the surface. For a reference, we have also obtained a bulk spectrum obtained at the midpoint of the cross-sectional sample. As evident from these spectra (Fig. 6), there is no shift in L edges throughout the length of the film. Also, there is no significant variation in L_3/L_2 ratio. Based on these results, we conclude that the Fe valence does not change

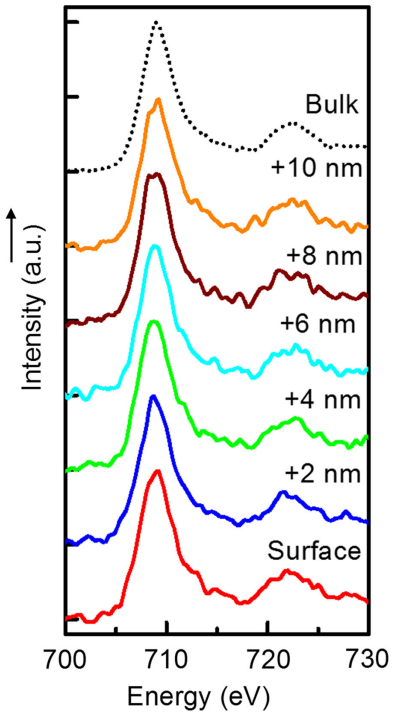

Fig. 6. Fe-L-edge EELS spectra as a function of distance from the surface side of the film to the bulk. The term "bulk" is used as a reference point situated approximately 500 nm from the surface. No significant change in L_3/L_2 ratio or a shift in the L edge is observed across the length of the cross-sectional sample (depth).

across the length of the film, including at the surface, consistent with the multiplet structure seen in TEY and TFY data. Similar Fe^{3+} valence values at the surface are reported in Ref. [35] for other iron garnets.

4. CONCLUSIONS

This article reports significant differences in the crystallographic structure and the XMCD and XAS between surface and bulk Fe^{3+} ions that play a central role in the nonreciprocal response in iron garnets. It is found that the distance between unit cells normal to the surface is reduced at the surface as compared to the bulk and a marked absence of Fe ions in some regions of the unit cell in the surface as compared to the bulk. These structural changes are accompanied by significant differences in TEY and TFY spectra, namely, suppression (enhancement) in TEY XMCD signals involving transitions from the $2p_{1/2}$ ($2p_{3/2}$) to 3d Fe^{3+} states with $j = 3/2$ (5/2) character, which we interpret as differences in electronic structure between surface and bulk states.

5. EXPERIMENTAL TECHNIQUES

A. S-TEM

The scanning-electron-transmission microscope used was a FEI Titan Themis aberration-corrected system. The imaging and spectroscopic measurements of the surface and the interior of the film were performed in scanning mode of the TEM with a point resolution of 0.8 Å. The microscope was fitted with superX quad detectors for fast mapping without losing any x-ray counts. For x-ray mapping, typically 20 μs dwell time and 100 picoamps of beam current were used. STEM and EDS data acquisition and image analysis was performed using ThermoFischer Velox. Electron energy loss spectroscopic measurements were performed in STEM mode. Spectrum images (SI)/EELS maps were obtained using the Gatan Quantum GIFTM system. The SIs were processed using DigitalMicrographTM software. The convergence and collection semi-angles were 16.9 mrad and 12.8 mrad, respectively. The maps were obtained at a step size of 1 nm/pixel, and EELS collection time was 1 second/pixel. The O-K edge at 538 eV was used to calibrate all the EELS spectra. Indexing and crystallographic calculations were performed using JEMS software.

B. XAS and XMCD

The incidence angle for the x-ray circularly polarized beam in our experiments at ANL ranged from 60 to 90 deg, with the detector angle fixed at 63.5 deg to the incident beam. XMCD measurements were done in helicity switching mode, both for magnetic field pointing along and opposite incident beam propagation direction. These measurements were done at room temperature. The XAS and XMCD experiments were performed using both TEY and total fluorescence TFY yield [24–26].

C. Samples

The Bi-substituted iron garnet films used for these experiments were grown by liquid-phase epitaxy on a (001)-oriented gadolinium gallium garnet substrate. These films were 2 μm thick. XMCD and XAS data were collected on three different samples obtained from the same wafer, with consistent results on all three samples. Two other samples from the same wafer were prepared by focused-ion-beam processing for S-TEM analysis. These cross-sectional lamellae were cut normal to the film surface for (001) and (111) zone plate analysis.

Funding. Air Force Research Laboratory (FA8650-17-C-5072); U.S. Department of Energy (DE-AC02-06CH11357).

Acknowledgment. The data was collected at Beamline 4-ID-C, which is operated by the Magnetic Materials Group in the X-ray Science Division (XSD) of the Advanced Photon Source, Argonne National Laboratory. This research used resources of the Advanced Photon Source, a U.S. Department of Energy (DOE) Office of Science User Facility operated for the DOE Office of Science by Argonne National Laboratory under Contract No. DE-AC02-06CH11357. The electron microscopy research was performed at the Applied Chemical and Morphological Analysis Laboratory at Michigan Technological University. The electron microscopy facility is supported by NSF MRI 1429232. ML and SSD acknowledge support from SRICO, Inc. and the Henes Center for Quantum Phenomena. This material is based in part on research sponsored by the Air Force Research Laboratory under contract number FA8650-17-C-5072. The views expressed are those of the authors and do not reflect the official policy or position of the Department of Defense or the U.S. Government. The authors also thank Thermo Fisher Scientific for the FIB processing of the lamellae for S-TEM analysis and S. Subramanian of II-VI, Inc. for valuable discussions.

Disclosures. The authors declare no conflicts of interest.

See Supplement 1 for supporting content.

REFERENCES

1. M. Levy, O. V. Borovkova, C. Sheidler, B. Blasiola, D. Karki, F. Jomard, M. A. Kozhaev, E. Popova, N. Keller, and V. I. Belotelov, "Faraday rotation in iron garnet films beyond elemental substitutions," Optica **6**, 642–645 (2019).
2. O. V. Borovkova, H. Hashim, M. A. Kozhaev, S. A. Dagesyan, A. Chakravarty, M. Levy, and V. I. Belotelov, "TMOKE as efficient tool for the magneto-optic analysis of ultra-thin magnetic films," Appl. Phys. Lett. **112**, 063101 (2018).
3. M. Levy, A. Chakravarty, H.-C. Huang, and R. M. Osgood, Jr., "Large magneto-optic enhancement in ultra-thin liquid-phase-epitaxy iron garnet films," Appl. Phys. Lett. **107**, 011104 (2015).
4. S. Geller and M. A. Gilleo, "Bismuth-containing garnets and their preparation," U.S. patent 3,281,363 (July 10, 1963), assignors to Bell Telephone Laboratories.
5. J. F. Dillon, Jr., "Light modulator," U.S. patent 2,974,568 (February 15, 1957), assigner to Bell Telephone Laboratories.
6. M. Gomi, H. Furuyama, and M. Abe, "Strong magneto-optical enhancement in highly Ce-substituted iron garnet films prepared by sputtering," J. Appl. Phys. **70**, 7065–7067 (1991).
7. G. F. Dionne, *Magnetic Oxides* (Springer, 2009), pp. 355–380.
8. B. J. H. Stadler and T. Mizumoto, "Integrated magneto-optical materials and isolators: a review," IEEE Photon. J. **6**, 1–15 (2014).
9. T. Mizumoto, R. Takei, and Y. Shoji, "Waveguide optical isolators for integrated optics," IEEE J. Quantum Electron. **48**, 252–260 (2012).
10. M. Levy, "The on-chip integration of magnetooptic waveguide isolators," IEEE J. Sel. Top. Quantum Electron. **8**, 1300–1306 (2002).
11. M.-C. Tien, T. Mizumoto, P. Pintus, H. Kromer, and J. E. Bowers, "Silicon ring isolators with bonded nonreciprocal magneto-optic garnets," Opt. Express **19**, 11740–11745 (2011).
12. P. Pintus, D. Huang, C. Zhang, Y. Shoji, T. Mizumoto, and J. E. Bowers, "Microring-based optical isolator and circulator with integrated electromagnet for silicon photonics," J. Lightwave Technol. **35**, 1429–1437 (2017).
13. M. Levy, H. C. Yang, M. J. Steel, and J. Fujita, "Flat top response in one-dimensional magnetic photonic band gap structures with Faraday rotation enhancement," J. Lightwave Technol. **19**, 1964–1969 (2001).
14. M. Levy, X. Huang, R. Li, H. C. Yang, and H. Bakhru, "Magneto-optic photonic crystals as optical waveguide structures," Proc. SPIE **5515**, 30–41 (2004).
15. M. Levy, "Nanomagnetic route to bias-magnet-free, on-chip Faraday rotators," J. Opt. Soc. Am. B **22**, 254–260 (2005).
16. M. Levy and R. Li, "Polarization rotation enhancement and scattering mechanisms in waveguide magnetophotonic crystals," Appl. Phys. Lett. **89**, 121113 (2006).
17. R. Li and M. Levy, "Bragg grating magnetic photonic crystal waveguides," Appl. Phys. Lett. **86**, 251102 (2005).
18. M. J. Steel, M. Levy, and R. M. Osgood, Jr., "High transmission enhanced Faraday rotation in one-dimensional photonic crystals with defects," IEEE Photon. Technol. Lett. **12**, 1171–1173 (2000).
19. M. J. Steel, M. Levy, and R. M. Osgood, Jr., "Photonic bandgaps with defects and the enhancement of Faraday rotation," J. Lightwave Technol. **18**, 1297–1308 (2000).
20. M. J. Steel, M. Levy, and R. M. Osgood, Jr., "Large magneto-optical Kerr rotation with high reflectivity from photonic bandgap structures with defects," J. Lightwave Technol. **18**, 1289–1296 (2000).
21. M. Inoue, K. Arai, T. Fujii, and M. Abe, "One-dimensional magnetophotonic crystals," J. Appl. Phys. **85**, 5768–5770 (1999).
22. M. Inoue, K. I. Arai, T. Fujii, and M. Abe, "Magneto-optical properties of one-dimensional photonic crystals composed of magnetic and dielectric layers," J. Appl. Phys. **83**, 6768–6770 (1998).
23. M. Inoue and T. Fujii, "A theoretical analysis of magneto-optical Faraday effect of YIG films with random multilayer structures," J. Appl. Phys. **81**, 5659–5661 (1997).
24. A. Di Cicco, A. Giglia, R. Gunnella, S. L. Koch, F. Mueller, F. Nobili, M. Pasqualini, S. Passerini, R. Tossici, and A. Witkowska, "SEI growth and depth profiling on ZFO electrodes by soft x-ray absorption spectroscopy," Adv. Energy Mater. **5**, 1500642 (2015).
25. A. Rousi, C. Raisch, A. Verna, B. A. Davidson, J. Fujii, R. Kleiner, and D. Koelle, "Electron sampling depth and saturation effects in perovskite films investigated by soft x-ray absorption spectroscopy," Phys. Rev. B **90**, 125120 (2014).
26. S. Tardif, "Nanocolonnes de GeMn : propriétés magnétiques et structurales à la lumiére du synchrotron," https://tel.archives-ouvertes.fr/tel-00585130.
27. B. Fultz and J. Howe, *Transmission Electron Microscopy and Diffractometry of Materials*, 4th ed. (Springer, 2013).
28. S. J. Pennycook, "Z-contrast STEM for materials science," Ultramicroscopy **30**, 58–69 (1989).
29. N. W. Ashcroft and N. D. Mermin, *Solid State Physics* (Holt, Rinehart and Winston, 1976).
30. D. Haskel, FLUO: Correcting XANES for self-absorption effects, https://www3.aps.anl.gov/haskel/fluo.html.
31. P. Rudolf, F. Sette, L. H. Tjeng, G. Meigs, and C. T. Chen, "Magnetic moments in a gadolinium iron garnet studied by soft-X-ray magnetic circular dichroism," J. Mag. Mag. Mater. **109**, 109–112 (1992).
32. L.-C. Duda, J. Stöhr, D. C. Mancini, A. Nilsson, N. Wassdahl, J. Nordgren, and M. G. Samant, "Magnetic dichroism in $L_{2,3}$ emission of Fe, Co, and Ni following energy-dependent excitation with circularly polarized x rays," Phys. Rev. B **50**, 16758–16761 (1994).
33. J. van Elp, G. Peng, Z. H. Zhou, S. Mukund, and M. W. W. Adams, "Soft-x-ray magnetic circular dichroism on a paramagnetic two-iron system," Phys. Rev. B **53**, 2523–2527 (1996).
34. G. Cressey, C. M. B. Henderson, and G. van der Laan, "Use of L-edge x-ray absorption spectroscopy to characterize multiple valence states of 3d transition metals; a new probe for mineralogical and geochemical research," Phys. Chem. Miner. **20**, 111–119 (1993).
35. E. Popova, A. Shengelaya, D. Daraselia, D. Japaridze, S. Cherifi-Hertel, L. Bocher, A. Gloter, O. Stéphan, Y. Dumont, and N. Keller, "Bismuth iron garnet $Bi_3Fe_5O_{12}$: a room temperature magnetoelectric material," Appl. Phys. Lett. **110**, 142404 (2017).